

Ferromagnetism and metallic state in digital (Ga,Mn)As heterostructures

Stefano Sanvito*

Physics Department, Trinity College, Dublin 2, Ireland

(Received 23 May 2003; published 26 August 2003)

We present an extensive density-functional theory study of the electronic, magnetic, and transport properties of GaAs and AlAs digital ferromagnetic heterostructures. These can be obtained by δ doping with Mn the GaAs layers of a GaAs/AlAs superlattice. Our analysis spans a range of Mn concentrations and considers the presence of compensating defects such as As antisites. In the defect-free case all the heterostructures studied present a half-metallic electronic structure. In contrast, when As antisites are present the half-metallic state is destroyed and the heterostructures behave as dirty planar metals. In this case they show a large p -type metallic conductance in the Mn plane mainly due to majority spin electrons, and an n -type hopping like conductance in the GaAs planes mainly due to minority spin electrons. This suggests that if the As antisites can be kept far from the Mn planes, spatial separation of the different spin currents can be achieved. Finally, we show that in the case of AlAs/(Ga,Mn)As digital ferromagnetic heterostructures the AlAs/GaAs valence band offset produces an additional confining potential for the holes responsible for the ferromagnetism. Therefore the ferromagnetic coupling between the Mn ions becomes larger and more robust to the presence of As antisites.

DOI: 10.1103/PhysRevB.68.054425

PACS number(s): 75.50.Pp, 71.20.Nr, 71.15.Mb

I. INTRODUCTION

(Ga,Mn)As (Ref. 1) is the prototype of a new class of magnetic materials named diluted magnetic semiconductors (DMS).^{2,3} These are obtained by doping ordinary semiconductors with transition metals. In the case of (Ga,Mn)As the Mn ions occupy the Ga sites and provide both localized spins ($S=5/2$) and holes. The spin holes are then antiferromagnetically coupled to the Mn ions and this gives rise to hole-mediated long-range ferromagnetism via a Zener-like mechanism.⁴

The potential impact of this material on the semiconductor industry is huge, since it opens the possibility of adding ferromagnetism to the AlAs/GaAs system, an important step toward the implementation of the spin degree of freedom in an electronic device.⁵ To date several concept devices have been demonstrated, including spin-polarized light emitters⁶ and electrically controlled ferromagnetism,⁷ and one can envision (Ga,Mn)As among the building blocks for a spin-based quantum computer scheme.⁸

Despite these indisputable successes the critical temperature (T_C) of (Ga,Mn)As hardly exceeds 110 K (Refs. 2 and 3) and this poses severe limitations to future commercial applications. At present low-temperature annealing processing has allowed an increase of the Curie temperature from 110 K to about 170 K,^{9,10} but room-temperature ferromagnetic (Ga,Mn)As appears difficult to produce. However, these recent annealing experiments have demonstrated an important point: the low critical temperature of (Ga,Mn)As is not an intrinsic limitation of the material, but is affected by the inability to control the Mn and holes concentration independently.

A possible way to improve the control over the electronic and magnetic interactions is to produce magnetic semiconductor superlattices. These are the digital ferromagnetic heterostructures (DFH), which are obtained by δ doping with Mn a low-temperature GaAs MBE-grown layer.¹¹ Here Mn concentrations as high as 50% are obtained in a few (typi-

cally 2 to 3) GaAs monolayers and one may expect correspondingly higher large Curie temperatures. However, these structures show properties rather different from those of their random alloy counterparts. Here we report the most relevant experimental findings.

(1) The Curie temperature is rather low (~ 50 K) and independent of the separation between the Mn planes.¹¹ T_C usually decays with increasing the thickness of the GaAs layer separating the MnAs submonolayers, and saturates for thicknesses larger than ~ 50 GaAs monolayers. The saturation is unexpected according to the mean-field model for three-dimensional systems, since the total Mn concentration in the sample decreases with the increase of the GaAs thickness.⁴ This separation dependence suggests that DFH behave like planar systems.

(2) Hall measurements in the direction parallel to the MnAs planes show an anomalous Hall effect for undoped samples, which disappears upon Be doping.^{12,13} Large Shubnikov–de Haas oscillations are found in doped samples, although surprisingly the carrier densities extracted from the Hall coefficient and from the Shubnikov–de Haas oscillations are different. This suggests that two different carrier types could be present in the system.

(3) There is a correlation between metallicity and Curie temperature. In low- T_C samples the transport is given by activated hole conduction and this is consistent with variable range hopping in two dimensions.^{14–16} In contrast, in the only DFH to date showing T_C around room temperature the transport is p type and metallic.¹⁷ However, in these latter structures made from (Ga,Mn)Sb two phases may be present,^{15,17} with a diluted phase responsible for the ferromagnetism below 40 K and a zinc blende MnSb phase responsible for the room-temperature ferromagnetism.

(4) GaAs/AlAs band engineering and spatial selective doping^{18,19} allow the enhancement of the T_C in AlAs/(Ga,Mn)As DFH with respect to their GaAs/(Ga,Mn)As counterparts. This enhancement is correlated with the en-

hanced hole concentration in the Mn layers and to the achievement of metallic conductance.

Finally, we point out that some of the aspects described above are common to other δ -doped structures. For instance, it has been recently demonstrated²⁰ that Be δ -doped low-temperature GaAs undergoes an insulator to metal transition as the Be concentration is enhanced. In this case the transport changes from n -type thermally activated to p -type metallic. The first is reported for small Be concentrations and is due to the hopping between As antisite levels in the GaAs region, while the second dominates at large Be concentrations and is due to extended hole states in the Be-rich region.

From this brief overview it is clear that DFH present rather rich and complex physics, which calls for an extensive theoretical analysis. So far the magnetic properties of DFH have been studied only within the mean-field approach,^{21,22} while the transport has been investigated solely in the ballistic limit for the case of 100% Mn doping in the plane.²³ Here we report an extensive *ab initio* study of the electronic, magnetic, and transport properties of both GaAs/(Ga,Mn)As and AlAs/(Ga,Mn)As DFH, for various Mn concentrations and As antisite doping levels.

The paper is organized as follows. In the following section we describe our computational technique and motivate the approximations made. Then we investigate the properties of GaAs/(Ga,Mn)As DFH, the effects of As antisites, and the properties of AlAs/(Ga,Mn)As DFH. Finally, we conclude and suggest ways to manipulate the properties of DFH.

II. COMPUTATIONAL TECHNIQUE

We perform density-functional theory (DFT) (Ref. 24) calculations within the local spin-density approximation (LSDA). The use of LSDA for DMS is very well documented,²⁵ and it provides a good description of the main physics of (Ga,Mn)As. Recently we have demonstrated²⁶ that self-interaction corrections to the LSDA do not strongly affect the band structure of (Ga,Mn)As, although they lead to strong localization and orbital ordering of the Mn d shell in (Ga,Mn)N. For this reason we choose to work within the LSDA.

Our numerical implementation, contained in the code SIESTA,^{27,28} uses pseudopotentials and a highly optimized localized atomic orbital basis set. These two aspects make SIESTA extremely suitable for handling systems with a large number of atoms in the unit cell without a significant loss of accuracy. The drawback is that both the pseudopotentials and the basis set must be accurately optimized.

First we consider the pseudopotentials. We use well-tested scalar relativistic Troullier-Martins pseudopotentials²⁹ with nonlinear core corrections³⁰ and Kleinman-Bylander factorization.³¹ The eigenvalues for the valence electrons of the free atom are compared with those generated for an all-electron calculation for different atomic and ionic configurations. Then we perform total-energy calculations for elementary solids comparing the lattice constant, the bulk modulus, and the band structure with reference calculations. These are performed with a well-converged basis set. Note that this is quite a delicate procedure, since with localized orbital basis

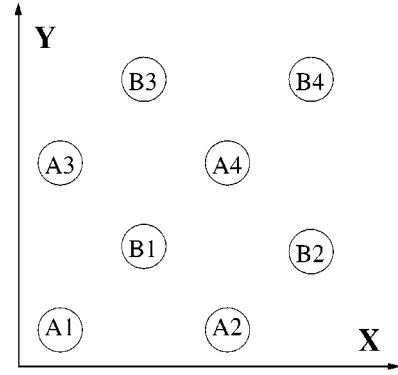


FIG. 1. The eight possible positions of the Mn ions in the supercell.

sets the variational principle is not governed by a single-parameter such as the cutoff energy with plane waves.

Finally an optimized basis set is selected. The basis functions in SIESTA are the product of an angular function with a given angular momentum, and a radial numerical function. This latter is constructed as the DFT solution of the free pseudo atom with an additional hard-wall confining potential. Furthermore, in order to enhance the variational freedom, several radial functions (“zetas”) for the same angular momentum are constructed with the “split valence” scheme.³² In the case of (Ga,Mn)As the crucial aspect is to introduce several zetas for the Mn d orbitals, and the criterion we have adopted is that of reproducing the physics of the d shell of Mn in MnAs. More details are given in Ref. 33. Here we only mention that the same procedure has been adopted for the Al pseudopotential and basis set. These have been checked for both metallic Al and zinc blende AlAs. The reference configuration for the pseudopotential is $3s^23p^1$ with cutoff radii 1.90 and 1.80 a.u., respectively, for the s and p shells. Finally the basis set for Al has two basis functions for both s and p electrons, with the same cutoff radius of 6.0 a.u. and the “split norm” parameter is 0.15.²⁸

All the calculations presented here are performed within a supercell scheme. Our supercell is constructed from a $2 \times 2 \times 3$ zinc blende cubic cell (lattice constant $a_0 = 5.65 \text{ \AA}$) and contains 96 atoms in total. We mimic a digital ferromagnetic heterostructure DFH by replacing Ga with Mn ions only in one of the GaAs planes. We use periodic boundary conditions in all directions sampling 18 k points in the supercell Brillouin zone. This corresponds to a (Ga,Mn)As/GaAs superlattice in which the (Ga,Mn)As planes are separated by six GaAs monolayers (16.95 \AA). In this supercell the Mn ions can occupy only eight possible positions in plane. These are arranged into two simple cubic lattices translated with respect to each other along the diagonal of the xy plane. Since the exact positions of the Mn ions are rather important in determining the electronic structure, these are schematically presented in Fig. 1.

III. (Ga,Mn)As DFH

In this section we analyze the effects of the Mn concentration on the electronic properties of (Ga,Mn)As DFH, by

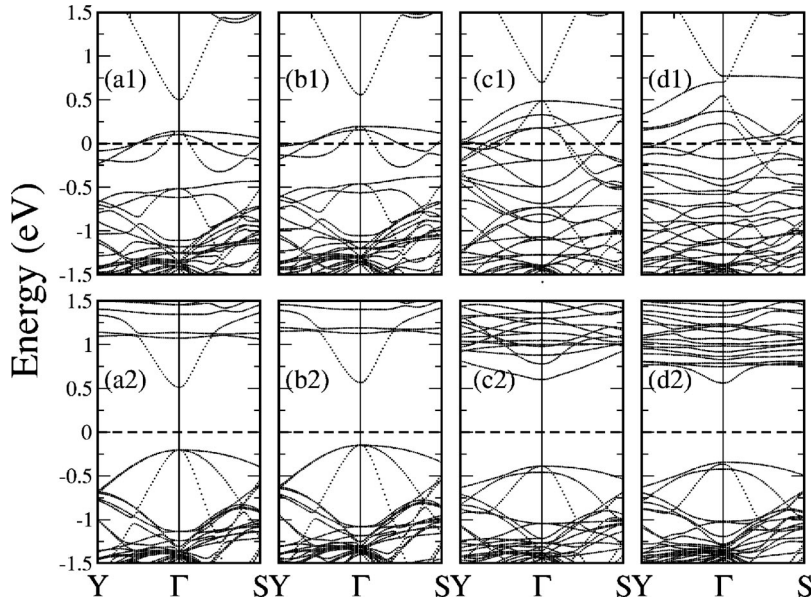


FIG. 2. Band structure of the (Ga,Mn)As/GaAs DFH described in the text as a function of the Mn concentration. The directions are parallel to the MnAs planes. The upper panels correspond to the majority spin band and the lower to the minority. The Mn concentrations are (a) 12.5%, (b) 25%, (c) and (d) 50%. In the case of 50% concentration we consider two different arrangements of the Mn atoms: (c) A1, A2, A3, A4, (d) A1, A2, A3, B1.

calculating the band structure, the DFT total potential, the strength of the ferromagnetic (FM) coupling, and the transport properties. Our main aim is to monitor the evolution of these quantities as a function of the Mn concentration in the (Ga,Mn)As plane. In particular, we want to establish whether there is a correlation between the Mn concentration and the metallicity of the system.

A. Band structure

In Fig. 2 we present the band structure of our (Ga,Mn)As/GaAs DFH for Mn concentrations of 12.5%, 25%, and 50%. In Figs. 2(a), 2(b), and 2(c), only the sites belonging to one of the two cubic sublattices in the plane are occupied. This maximizes the mean Mn-Mn separation. In contrast, in Fig. 2(d) sites belonging to both the lattices are occupied (namely, A1, A2, A3, and B1). Here we plot the bands only along two directions parallel to the (Ga,Mn)As plane, since in the perpendicular direction these are very similar to the case of MnAs planes embedded in GaAs (Ref. 23) and they do not change significantly with the Mn concentration. In contrast for directions parallel to the Mn planes, we expect a transition from the band structure of a (Ga,Mn)As random alloy to the metallic band structure of a zinc blende MnAs plane.²³ This is indeed the behavior observed in Fig. 2. If one increases the Mn concentration from 12.5% to 50% [from (a) to (b) to (c)] the Fermi level shifts downward in energy ending up deep in the majority spin valence band. At the same time also the spin splitting of the valence band increases. Note that the DFH behaves as a half-metal at every concentration. The magnetic moment of the supercell therefore is always $4\mu_B \times N_{\text{Mn}}$ where N_{Mn} is the number of Mn atoms in the cell. Mülliken population analysis^{33,34} shows an orbital population for the Mn d shell of ~ 4.7 for the majority spin electrons and of ~ 0.8 for the minority, although both depend on the specific spatial arrangement of the Mn ions. These aspects are consistent with the picture of Mn as a single

acceptor in GaAs. The Mn ions are in a d^5 state with an associated antiferromagnetically coupled hole, as for the case of the random alloys.³³

However, the situation of Fig. 2(d) is in stark contrast with this picture. In this case the Mn concentration is still 50% but three of the four Mn ions in the plane occupy nearest-neighbor positions. The band gap in the majority spin band closes and the material is a half-metal with a completely metallic majority spin band. This suggests that the actual position of the Mn atoms in the plane is crucial in determining the electronic properties. The same sensitivity of the electronic structure to the position of the Mn ions is also present in the random alloys.³⁵ However, this generally does not lead to a strong distortion of the band structure, and the bands obtained for Mn ions diluted in the supercell or occupying nearest-neighbor positions are quite similar. In DFH the planar arrangement of the Mn ions makes the system more confined, and therefore more sensitive to inhomogeneities. This of course drastically affects the scattering properties of electrons in the (Ga,Mn)As planes, as we will show in the following sections.

B. DFT potential

One fundamental question for understanding the physics of DFH is: “are the spin carriers confined in the (Ga,Mn)As plane or do they spread over the GaAs spacer?”. In order to answer this question it is useful to investigate the behavior of the total DFT potential along the superlattice direction z . This of course has the same periodicity as the atomic lattice. However, we are not interested in the potential at the atomic scale, and instead we perform a “macroscopic average”.³⁶ The macroscopic average is obtained by first taking a planar average and then by averaging the result over the period of a GaAs monolayer along the superlattice direction. The resulting z -dependent potential is that felt by an electron with long wavelength at a density small enough not to perturb signifi-

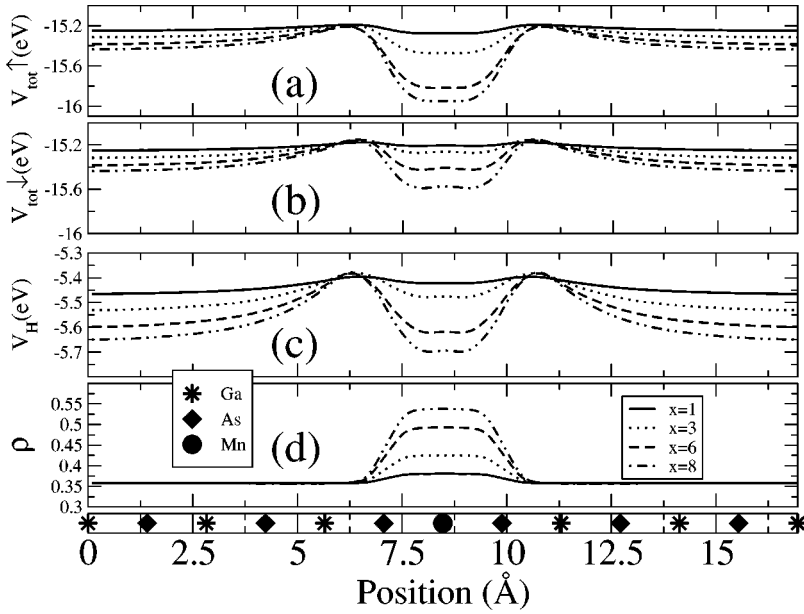


FIG. 3. Macroscopic average of (a) the total DFT potential for majority spins, (b) the total DFT potential for minority spins, (c) the Hartree potential, and the (d) charge-density distribution as a function of the position along the superlattice direction, for different Mn concentrations (x is the number of Mn ions in the plane).

cantly the potential. Therefore this can be interpreted as the effective z -dependent potential in the spirit of the envelope function approximation.

In Fig. 3 we plot the macroscopic average for the total DFT potential, the Hartree potential, and the charge-density distribution as a function of the position along the superlattice direction for different Mn concentrations. Notice first that there is indeed a confining potential in the Mn plane. The charge density is unevenly distributed along the superlattice and accumulates in the Mn plane. This is consistent with the picture of the Mn ions that we have given in the past,³³ in which the majority spin hole is nearly bound to the Mn ion while the minority feels a much weaker potential.

The z -dependent total potential is strongly spin dependent. Generally, it has a double well structure, with two potential minima, located in the (Ga,Mn)As plane and in the GaAs spacer, respectively. These are separated by a potential barrier that grows if the Mn concentration in the plane increases. We further investigate the nature of the confining potential by calculating its evolution upon increasing the Mn doping. For this purpose we define Δ_1^{σ} and Δ_2^{σ} as the energy minima in the (Ga,Mn)As plane and the GaAs spacer, respectively, measured with respect to the top of the energy barrier (see Fig. 4). σ is the spin index and \uparrow (\downarrow) indicates the majority (minority) spin electrons. We denote as Δ_1^H and Δ_2^H the same quantities for the Hartree potential.

In Fig. 5 we present these quantities as a function of the number of Mn ions in the Mn plane (the maximum number is 8). First we notice that for minority spins both Δ_1^{\downarrow} and Δ_2^{\downarrow} mimic closely the behavior of the Hartree potential [Figs. 5(a), and 5(b)]. This means that the DFT potential for the minority spins is largely electrostatic with small contributions from the exchange part. In contrast Δ_1^{\uparrow} for the majority electrons deviates strongly from the behavior of its electrostatic component, and the deviation increases as the Mn concentration is enhanced.

If we now compare Δ_1 with Δ_2 for the two spin species we find a rather different behavior. For the majority spin

electrons [Fig. 5(c)] $\Delta_1 > \Delta_2$ at all Mn concentrations. Furthermore, the difference $\Delta_1 - \Delta_2$ increases with increasing the Mn concentration. This means that the minimum in the (Ga,Mn)As plane is always the lower of the minima for majority electrons and it becomes more stable as the Mn concentration increases.

In contrast, for the minority electrons there is no striking difference between Δ_1 and Δ_2 , meaning that they are less confined in the (Ga,Mn)As plane [see Fig. 5(d)]. It is also interesting to point out that $\Delta_2 > \Delta_1$ at low Mn concentration but there is a crossover for doping of the order of 50%. This is suggestive of the fact that the confinement of minority electrons switches from the GaAs to the (Ga,Mn)As region upon the increase of Mn concentration. Of course, there are no empty minority spin states at the Fermi level and therefore in these structures the minority spins contribute little to the electron transport. However, in the case of additional doping (for instance by intrinsic As antisites, As_{Ga}) an impurity band may form at the Fermi level, opening a transport channel in the minority subband. The potential described here suggests that those electrons will hardly distribute over the (Ga,Mn)As plane at low doping but they will invade the

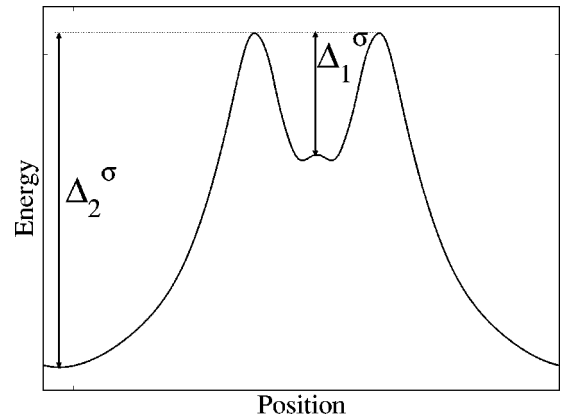


FIG. 4. Definition of Δ_1^{σ} and Δ_2^{σ} .

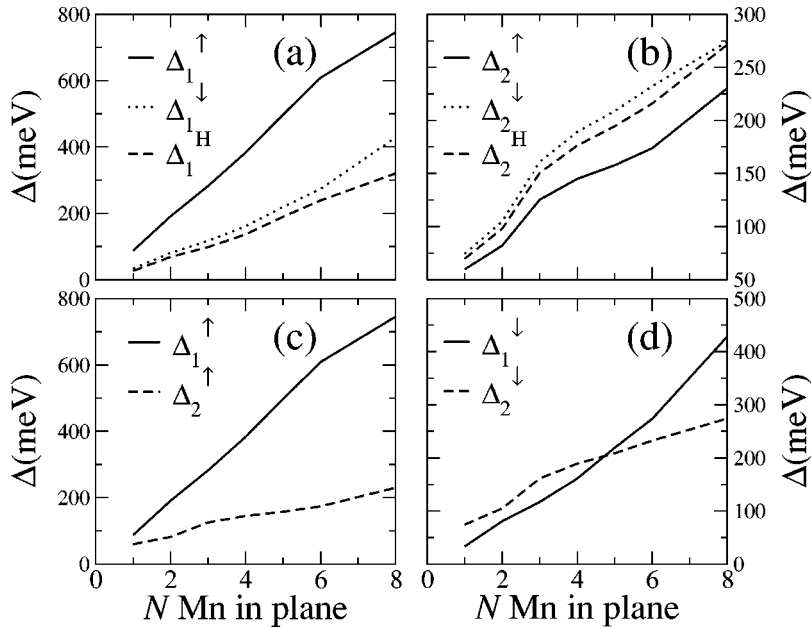


FIG. 5. Δ_1^σ , Δ_2^σ , Δ_1^H , and Δ_2^H as a function of the Mn concentration in the (Ga,Mn)As plane.

(Ga,Mn)As region at large Mn doping. For this reason we expect a spatial separation of the spin currents [majority spin in the (Ga,Mn)As plane, and minority spin in the GaAs spacer] for low concentrations, and strong spin mixing at higher concentrations.

C. Stability of the ferromagnetic state

In this section we investigate the strength of the ferromagnetic coupling in (Ga,Mn)As DFH, and in particular we discuss how the coupling depends on Mn doping. The relevant quantity to investigate is the energy difference $\Delta_{FA} = E_{AF} - E_{FM}$ between the total energy of the antiferromagnetic (E_{AF}) and the ferromagnetic (E_{FM}) configurations of the supercell. Here we investigate the case of 25%, 37.5%, and 50% Mn doping in the plane, where, respectively two, three, and four Mn ions are present in the supercell. This gives us some freedom to arrange the Mn ions in different ways and to investigate different antiferromagnetic configurations. A summary of the cases studied is presented in Table I.

We ran a total energy calculation for each of the configurations of Table I, and fit our calculations to a third nearest-neighbors Heisenberg model, in which the total energy E is expressed as

$$E = - \sum_{i < j}^{nn} J_{ij} \vec{S}_i \cdot \vec{S}_j. \quad (1)$$

J_{ij} are the exchange constants, \vec{S}_i is the spin of the i th Mn ions, and the sum runs up to third nearest neighbors. The results of this fit are presented in Table II, where by convention we use $|\vec{S}| = 5/2$. Note that in our fitting procedure we have more configurations than parameters, and it is remarkable to observe that the fit is generally very good. From the table it is clear that the first nearest-neighbor coupling constant J_1 is responsible for most of the coupling which decays rapidly with the Mn-Mn separation. It is also interesting to

note that the second nearest-neighbor coupling J_2 is small for all the concentrations studied. Remarkably, all the coupling constants are strongly dependent on the Mn concentration in the plane, and they decay quickly as this is increased. This decay, which is particularly severe for the first nearest-neighbor coupling constant, is in stark contrast with the expectations of RKKY-like (RKKY, Ruderman-Kittel-Kasuya-Yosida) theories in which the J 's increase as $x^{1/3}$ at zero temperature.³⁷ However, it is consistent with previous DFT-LDA calculations³⁸ for DMS random alloys, and illustrates

TABLE I. Summary table of the different magnetic configurations studied. The labels for the positions of the Mn ions are those of Fig. 1.

[Mn] Configuration (%)		Position				
		A1	A2	A3	A4	B1
25	FM ₁	↑				↑
25	AFM ₁	↑				↓
25	FM ₂	↑	↑			
25	AFM ₂	↑	↓			
25	FM ₃	↑			↑	
25	AFM ₃	↑			↓	
37.5	FM ₁	↑		↑	↑	
37.5	AFM ₁	↑		↑	↓	
37.5	AFM ₂	↑		↓	↑	
37.5	FM _{1n}	↑		↑		↑
37.5	AFM _{1n}	↑		↑		↓
50	FM ₁	↑	↑	↑	↑	
50	AFM ₁	↑	↓	↓	↑	
50	AFM ₂	↑	↓	↑	↑	
50	AFM ₃	↑	↑	↓	↓	
50	FM _{1n}	↑	↑	↑		↑
50	AFM _{1n}	↑	↑	↑		↓
50	AFM _{2n}	↓	↑	↑		↑
50	AFM _{3n}	↑	↑	↓		↓

TABLE II. J_1 , J_2 , and J_3 from the total-energy calculations for the configurations of Table I. The units are meV.

[Mn] in plane	J_1	J_2	J_3	$x\sum_i J_i$
$x=0.25$	23.3	2.9	5.6	7.95
$x=0.375$	19.8	1.4	4.9	9.8
$x=0.50$	13.3	0.9	4.5	9.35

once again the critical dependence of the Mn-Mn ferromagnetic coupling on the local chemical environment.

In order to put our calculations in perspective, next we estimate the ferromagnetic Curie temperature T_C of the system for different Mn concentrations. This can be simply obtained by using the mean-field expression for a three-dimensional Heisenberg model, which reads

$$T_C k_B = \frac{2}{3} S^2 n_{\text{Mn}} \sum_i J_i, \quad (2)$$

where n_{Mn} is the Mn concentration and the sum runs over all the cation sites. This is a rather crude approximation and a complete thermodynamic theory should include the elementary spin excitations.^{39,40} Moreover, in the present case the Mn concentration is not a well-defined quantity since the (Ga,Mn)As region cannot be separated from the GaAs region. Roughly speaking, one should consider the volume of (Ga,Mn)As to be the region around the Mn ions as thick as the range of the relative confining potential (see Fig. 3). This quantity is not clearly defined. Therefore, assuming that the (Ga,Mn)As volume does not depend on the Mn concentration, we prefer to evaluate only the following ‘‘magnetic energy’’:

$$E_{\text{mag}} = x \sum_i J_i, \quad (3)$$

which is proportional to the Curie temperature.

From Table II one notes that E_{mag} has a nonmonotonic dependence on the Mn concentration, presenting a maximum for $x=0.375$. Such behavior is generally observed in DMS random alloys, for which there is a maximum of T_C upon Mn doping, followed by a sharp decay for large Mn concentrations (above $x=0.05$).^{2,3} This usually coincides with the loss of the metallic state. In contrast, in DFH made to date the situation seems to be reversed,¹¹ with a larger T_C for larger Mn concentrations. This apparently contradicts our predictions. However, two important aspects need to be considered. First in actual DFH the transport is through variable range hopping,¹⁶ while in our supercell calculations the system is ‘‘by definition’’ metallic. Second, DFH usually present very strong compensation. This indicates that a large number of donors, whose density is probably related to the in-plane Mn concentration, are present in the DFH. In the next sections we will investigate systematically both the transport properties and the effects of the presence of donors.

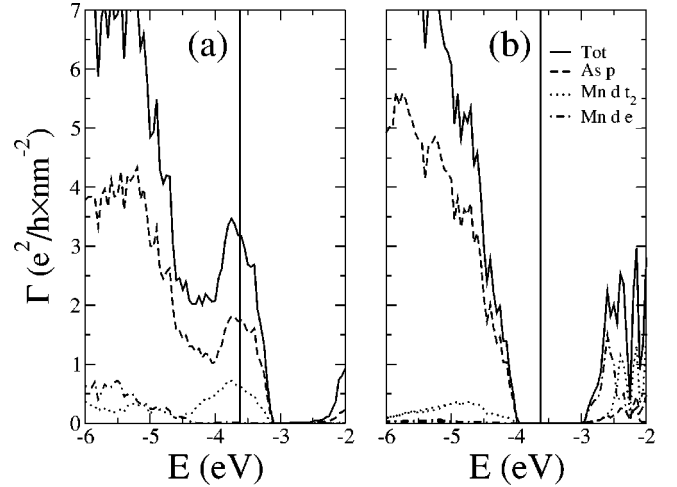


FIG. 6. Conductance as a function of energy for a 50% Mn DFH in the FM state. The Mn ions are uniformly spaced in the plane (configuration FM₁ of Table I). The vertical line indicates the position of the Fermi level. (a) Majority, (b) minority spins.

D. Ballistic transport

In this section we investigate the ballistic transport in DFH, with the aim of understanding the nature of the electronic states responsible for the conductance. The technique used is identical to that described in Refs. 23 and 41 and here we summarize only the main aspects. The transport is calculated by using the self-consistent tight-binding-like Hamiltonian and overlap matrix computed by SIESTA. The matrix elements are obtained from the self-consistent charge density by evaluating numerically both two- and three-center integrals.²⁸ Then we rewrite both the Hamiltonian and the overlap matrix in a tridiagonal form along the direction of the transport and use periodic boundary conditions along the other directions. Finally, the k -dependent transmission matrix $t_\sigma(k)$ for the spin direction σ is calculated by using our Green’s function technique,⁴¹ and the spin conductance Γ^σ in the Landauer-Büttiker formalism,⁴²

$$\Gamma^\sigma = \frac{e^2}{h} \sum_k^{\text{BZ}} \text{Tr} t_\sigma(k) t_\sigma(k)^\dagger, \quad (4)$$

where we integrate over the two-dimensional Brillouin zone in the plane orthogonal to the direction of the transport. Here we consider a two spin fluid model, where there is no mixing between the majority and minority spin currents.

We study transport only in the direction parallel to the Mn plane. In the orthogonal direction, in fact, the transport is mainly due to hopping between the Mn planes and it is strongly suppressed if these are sufficiently far apart.²³ In Fig. 6 we present the conductance as a function of energy for a 50% Mn supercell in the FM state, and with the Mn ions uniformly distributed in the plane (configuration FM₁ of Table I).

As expected from the band structure [Fig. 2(c)] the conductance as a function of energy shows a half-metallic behavior, with zero conductance for the minority spin band at the Fermi level. This 100% spin polarization of the conduc-

tance persists down to 0.5 eV from the Fermi energy, where minority states at the top of the valence band start contributing to the current. Turning our attention to the orbital contribution to the conductance it is important to observe that, at the Fermi level the current is entirely due to a mixture of As p and Mn $d t_2$ states. It is also interesting to note that non-negligible Mn d contributions are present in the majority spin band for energies down to 4 eV below the Fermi level. This is an indication of the strong p - d hybridization in the majority spin band, and in particular at its top. In contrast, the Mn d contribution to the conductance is almost negligible in the valence minority band, and Mn d states appear only for $E \geq -3$ eV, relative to the bottom of the conduction band.

This 100% spin polarization at the Fermi level is very encouraging for the potential use of DFH as spin injector for spintronics devices. However, it is crucial to investigate how this feature survives when compensating defects are present in the system.

IV. (Ga,Mn)As DFH: EFFECTS OF As_{Ga}

As in the case with the (Ga,Mn)As random alloys, DFH are also usually strongly compensated so that the hole concentration is considerably lower than the Mn concentration. It is generally accepted that the strong compensation is due to donors, most likely of intrinsic defects. In particular, both As antisites (As_{Ga}) (Refs. 3 and 35) and interstitial Mn (Mn_i) (Refs. 43 and 44) have been indicated as relevant compensating defects. The relative abundance of those donors probably depends on the growth conditions, the Mn concentration, and the post-growth processing. Since DFH are usually grown under large As overpressure,¹¹ we believe that in this case As antisites dominate. Here we investigate how the electronic properties of a 50% Mn DFH changes upon As_{Ga} doping.

A. Band structure

As in the preceding section, the band structure provides important information on the electronic properties of the DFH. In Fig. 7 we present the band structure for 50% in plane Mn DFH, where a single As_{Ga} is introduced into the GaAs spacer at midway between two consecutive (Ga,Mn)As planes (the total As_{Ga} concentration is $\sim 2\%$).

The most important feature of this band structure is that the half-metallic state is destroyed. This is due to the appearance of the As_{Ga} level in the minority spin band, and to the fact that the Fermi energy is pinned at this level. An As antisite in GaAs is a double donor with a doubly occupied deep level at midgap and an empty resonant state at the edge of the conduction band. These states have, respectively, the A and T_2 symmetries of the T_d point group.⁴⁵ In (Ga,Mn)As the density of such defects is generally rather large and they can give rise to the formation of narrow impurity bands. In addition, in the case of DFH it is likely that the As antisites will concentrate in the proximity of the Mn layers. This is confirmed by our total energy calculations, which show that there is an energy gain of approximately 0.9 eV when an As antisite moves from the middle of the cell to the Mn plane.

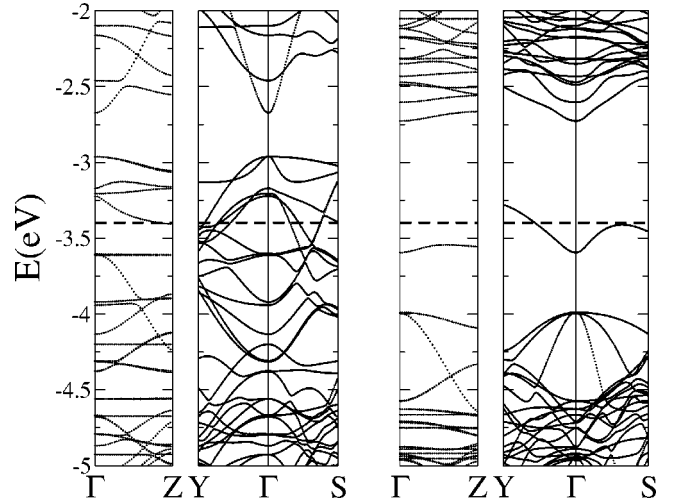


FIG. 7. Band structure for 50% Mn DFH where a single As_{Ga} is introduced in the GaAs spacer at midway between two (Ga,Mn)As planes. The directions are: (1) Y- Γ -S in the (Ga,Mn)As plane, (2) Γ -Z perpendicular to the (Ga,Mn)As plane. The horizontal line indicates the position of the Fermi level. On the left (right) we plot the majority (minority) band.

The total magnetic moment of such a unit cell is about $17.2\mu_B$ and depends weakly on the position of the As antisite with respect to the Mn plane [it is $17.33\mu_B$ when the As_{Ga} lies in the (Ga,Mn)As plane]. Assuming a rigid band model and considering that in absence of As antisites the magnetic moment of the cell is $16\mu_B$, we conclude that an As_{Ga} contributes 0.4 electrons to the minority band and 1.6 to the majority (we recall that one As_{Ga} also introduces an impurity state that can accommodate two electrons). Therefore the presence of one As antisite in such a unit cell has two main effects: (i) it compensates up to 1.6 holes in the majority spin band, and (ii) it opens a conduction channel at the Fermi level in the minority spin band. This is a crucial aspect for understanding the transport properties of such structures.

B. Transport in presence of As antisites

We calculate the in-plane ballistic conductance for a 50% Mn DFH with one As_{Ga} in the middle of the spacer and the Mn ions uniformly distributed in the plane (configuration FM_1). This is the same situation as in Fig. 6. The results are presented in Fig. 8, where again we have considered up to 100 k points in the transverse Brillouin zone.

The main difference with respect to the As_{Ga} -free case is the presence of a nonvanishing conductance for the minority spin electrons at the Fermi energy. This is entirely due to the As_{Ga} impurity band as pointed out in the preceding section, and of course destroys the half-metallic behavior of the spin current. The spin polarization of the current P , defined as

$$P = \frac{\Gamma^\uparrow - \Gamma^\downarrow}{\Gamma^\uparrow + \Gamma^\downarrow}, \quad (5)$$

where the conductances are taken at the Fermi level, drops from 100% in the defect-free case to about 60% in the present case.

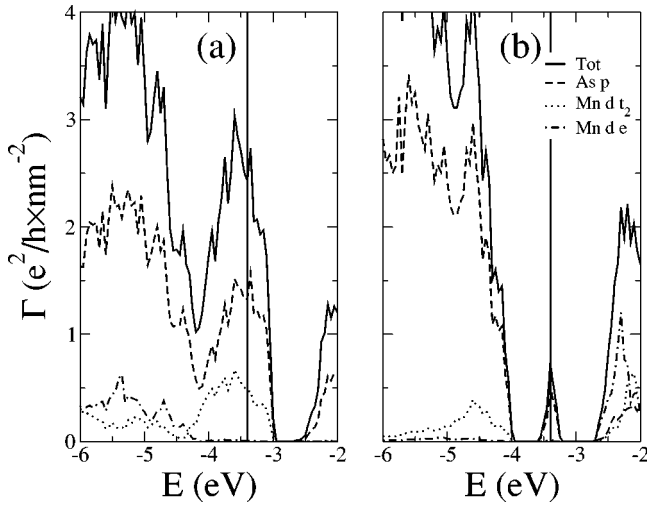


FIG. 8. Ballistic conductance as a function of energy for a 50% Mn DFH with one As_{Ga} in the middle of the unit cell, half way between two consecutive (Ga,Mn)As planes. The vertical line indicates the position of the Fermi level. (a) Majority, (b) minority spins.

However, the situation is rather different if we consider diffusive transport.⁴⁶ This is due to the different way in which the density of states and the group velocity contribute to the conductance in the ballistic and diffusive limits. In fact, in the ballistic limit the conductance of a uniform system can be obtained simply by summing up the number of scattering channels at the Fermi level

$$\Gamma^\sigma = \frac{e^2}{h} \sum_k^{\text{BZ}} 1 = \frac{e^2}{h} \sum_k^{\text{BZ}} N_k^\sigma v_k^\sigma = \frac{e^2}{h} \langle Nv \rangle^\sigma, \quad (6)$$

where N_k^σ and v_k^σ are, respectively, the density of state and the group velocity for a spin σ scattering channel, and the sum is performed over the two-dimensional Brillouin zone orthogonal to the transport direction. In contrast from the classical Boltzmann equation, one finds that the diffusive spin conductance is proportional to

$$\tau^\sigma \langle Nv^2 \rangle^\sigma = \tau^\sigma \sum_k N_k^\sigma v_k^{\sigma 2}, \quad (7)$$

where now the sum runs over the three-dimensional Fermi surface and τ^σ is the spin-dependent relaxation time.⁴⁶ This reflects the well-known fact that, while in the ballistic limit all the scattering channels contribute with e^2/h to the conductance independently from their group velocity, in the diffusive case the current is dominated by fast electrons because of the v^2 dependence.

If one assumes that the relaxation time is not dependent on the spin direction ($\tau^\uparrow = \tau^\downarrow$), then the spin polarization of the current in the diffusive limit can be written as

$$P_{\langle Nv^2 \rangle} = \frac{\langle Nv^2 \rangle^\uparrow - \langle Nv^2 \rangle^\downarrow}{\langle Nv^2 \rangle^\uparrow + \langle Nv^2 \rangle^\downarrow}. \quad (8)$$

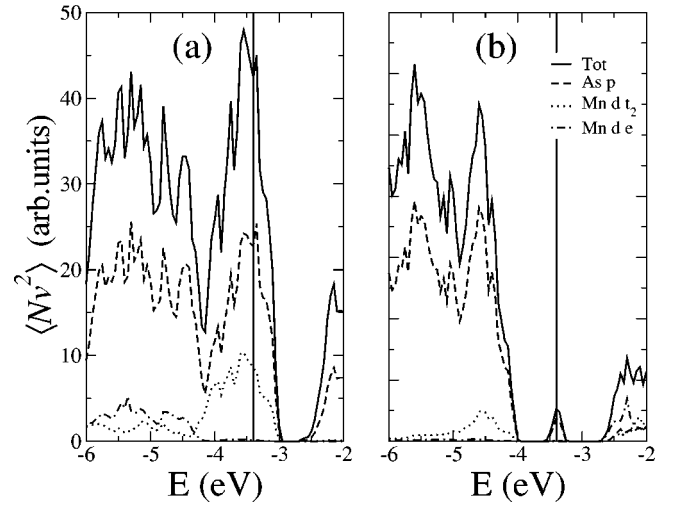


FIG. 9. $\langle Nv^2 \rangle$ as a function of energy for a 50% Mn DFH with one As_{Ga} in the middle of the unit cell, half way between two consecutive (Ga,Mn)As planes. The vertical line indicates the position of the Fermi level. (a) Majority, (b) minority spins.

In general P and $P_{\langle Nv^2 \rangle}$ are different, with $P_{\langle Nv^2 \rangle}$ larger if the difference in conductance for the two spin channels originates from a large Fermi velocity mismatch between the two spin bands. This is the case in the present DFH. In the majority band the Fermi surface is derived from the top of the GaAs valence band and the Fermi velocity is rather large. In contrast, the minority band Fermi surface is due to the As antisite impurity band and the Fermi velocity is quite small. Therefore, since in the diffusive limit the conductance is proportional to v^2 , we expect a much larger spin polarization of the current compared with the ballistic case.

In Fig. 9 we present $\langle Nv^2 \rangle$ as a function of energy for the same DFH as that of Fig. 8. The spin polarization at the Fermi energy is now 80%. Since in actual DFH the transport is due to hopping conductance,¹⁶ we can conclude that As antisites, although they destroy the half-metallic state, do not strongly affect the spin polarization of the current.

Finally, it is interesting to study the spatial distribution of the current across the DFH in the presence of As antisites. In Fig. 10 we present the real-space charge-density distribution, $\rho(\mathbf{r})$, calculated only for those states contributing to the conductance at the Fermi energy.²³ Strictly speaking this does not represent the current distribution in real space, but gives information on the spatial distribution of the conductance electrons' wave functions around E_F . The main feature of Fig. 10 is that there is a spacial separation between the two spin currents, with the majority spin current located near the Mn plane, and the minority current strongly localized around the As antisites. The first is evenly distributed and this is suggestive of a metalliclike behavior, while the second is strongly localized at the scattering center, suggesting a hoppinglike transport. Moreover, if we correlate the spin current with the relevant band structure (see Fig. 7), we notice that the majority spin current is holelike, while the minority is electronlike.

We also investigate how these features change when the As antisite moves toward the Mn plane. Although the con-

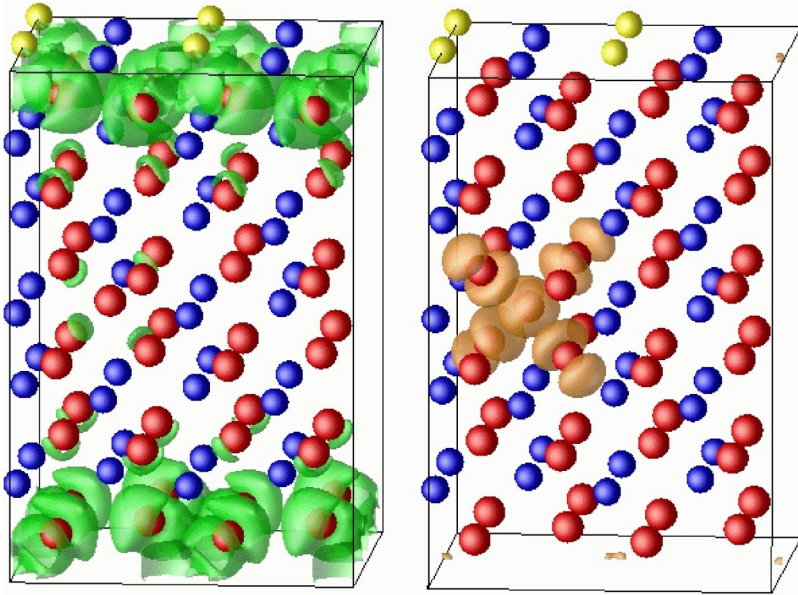


FIG. 10. Real-space distribution of the current. This is calculated as the charge-density distribution in real space of those scattering states contributing to the conductance at E_F .

ductance as a function of energy does not present any significant modifications with respect to the case of Fig. 7, the spacial distribution shows an increased participation of the As antisite in the majority spin conductance as it moves closer to the Mn plane. This suggests that As antisites can play an important rôle in spin relaxation processes within DFH.

In conclusion, our transport results suggest that, if there is no spin mixing, the transport is dominated by a p -type metalliclike majority spin current with a smaller contribution from an n -type hoppinglike minority spin current. Moreover, the two spin currents are spatially separated, preventing spin mixing, only if the As antisites are reasonably far from the Mn plane.

C. Fit to the Heisenberg model

We now investigate the stability of the ferromagnetic state when As antisites are present. We perform similar calculations to those described in Sec. III C, but this time we include one As_{Ga} in the unit cell. Since the relative position of the As_{Ga} with respect to the Mn ions is crucial in determining the electronic and magnetic properties,³⁵ we investigate how the coupling depends on the As antisite position along the superlattice direction.

In Fig. 11(a) we present the value of the exchange constant for first, second, and third nearest-neighbor couplings as a function of the position of the As antisite with respect to the Mn plane. In the same figure we also present the same values for the As antisite-free case and for the case of two As antisites (located, respectively, at $1/3$ and $2/3$ of the supercell along the superlattice direction).

From the figure it is clear that, in all cases, most of the coupling comes from nearest-neighbor interaction, which accounts on average for 75% of the total coupling $J_{tot} = \sum_i J_i$. Then there is a fast decay of the exchange coupling with separation. This coupling is therefore short range. Furthermore, it is very interesting to note that the second nearest-neighbor coupling (Mn ions at A1 and A2) is almost

negligible in all cases, and it sometimes assumes negative values. This suggests possible local antiferromagnetic coupling between the Mn ions as recently demonstrated experimentally.¹⁵

Turning our attention to the effect of As antisites, it is clear that these weakened the coupling between the Mn ions. This is expected since an As_{Ga} is a donor and therefore its presence partially compensates the free holes responsible for the long-range ferromagnetic coupling. However, our accurate supercell calculations bring additional interesting features. In agreement with the case of the random alloys (see Ref. 35), the actual position of the As antisite with respect to the Mn ions determines most of the properties. From Fig. 11 it is clear that the ferromagnetic coupling is weakened when the As antisite moves toward the Mn plane. In particular, the exchange constants for the cases when $z = 1/6$ and $z = 0$ are

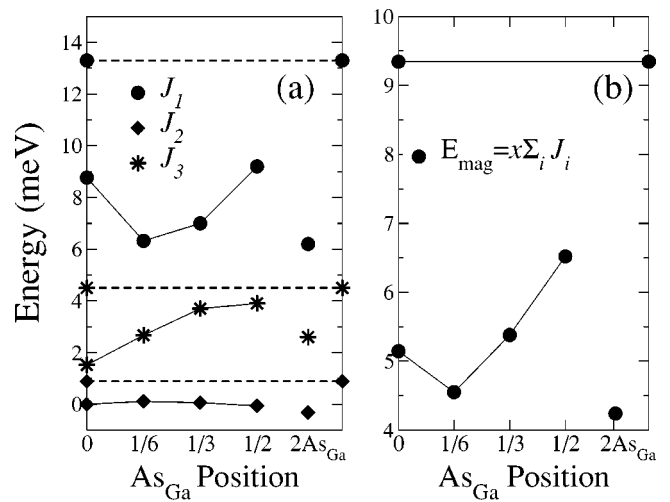


FIG. 11. (a) Exchange constants J_1 , J_2 , and J_3 and (b) magnetic energy E_{mag} of a DFH as a function of the position of the As antisite with respect to the Mn plane (in units of the superlattice period). We also include the case of two As antisites. The horizontal lines indicate the same quantities for the antisite-free case.

very similar to those of the case of two As antisites ($z = 1/3$ and $z = 2/3$). This feature can be understood by considering the potential profile discussed in the preceding section. In fact, the charge is strongly confined in the Mn plane with a potential barrier separating the plane from the GaAs region. Therefore it is natural to think that any perturbation in the GaAs region will only weakly affect the electronic configuration of the Mn plane, unless such a perturbation is spatially located in the vicinity of such a plane.

In the second half of Fig. 11 we present the magnetic energy $E_{\text{mag}} = x \sum_i J_i$ for the different cells investigated. As we pointed out previously, this quantity is proportional to the Curie temperature T_C . From the figure it is clear that E_{mag} depends sensitively on the presence of the As antisites and on their actual location. In particular, although we find the lowest value of E_{mag} in the case in which two As antisites are present, we also find that this is very similar to the case of a single As antisite located in close proximity to the Mn plane ($z = 1/6$ in the present case). Therefore we conclude that one can obtain high Curie temperatures, not only by avoiding the formation of intrinsic defects, but also by controlling their position with respect to the magnetic region.

Finally we make a few comments on the effect of disorder. Since in actual samples we are not able to control the exact position of the Mn ions with respect to each other, and since the Mn-Mn coupling is strongly dependent on the relative positions of the Mn ions and those of the As antisites, it is likely that there are regions of strong Mn-Mn coupling together with regions of weak or even antiferromagnetic coupling. This suggests that in addition to configurational disorder, magnetic disorder can also be present in DFH even at low temperatures. Therefore since the electrons (or holes) at the Fermi level have a rather large (metallic) density, and are strongly confined in a few atomic planes around the Mn ions, we can conclude that DFH have the electronic properties of highly resistive (dirty) metals. Turning the argument around, we conclude that the metallicity is crucial for the magnetic state of DFH, and that the most metallic samples are likely to show less magnetic disorder and therefore more robust magnetic properties.¹⁷

V. AlAs/(Ga,Mn)As HETEROSTRUCTURES

One of the main messages from the analysis done so far is that the exchange part of the DFT potential creates a strong confinement potential for the majority electrons in the Mn plane. In this section we investigate the effects of an additional confining potential, namely, that obtained by sandwiching a (Ga,Mn)As monolayer into the GaAs region of an AlAs/GaAs superlattice. Our expectation is that the AlAs/GaAs band alignment will further confine the spin holes in the proximity of the Mn ions, therefore enhancing the exchange coupling.

A. GaAs/AlAs band alignment

Before considering the Mn-doped case we first illustrate the general band alignment of an AlAs/GaAs superlattice, as obtained from our DFT calculations. The valence-band offset Δ is calculated as suggested by Baroni *et al.*³⁶ as

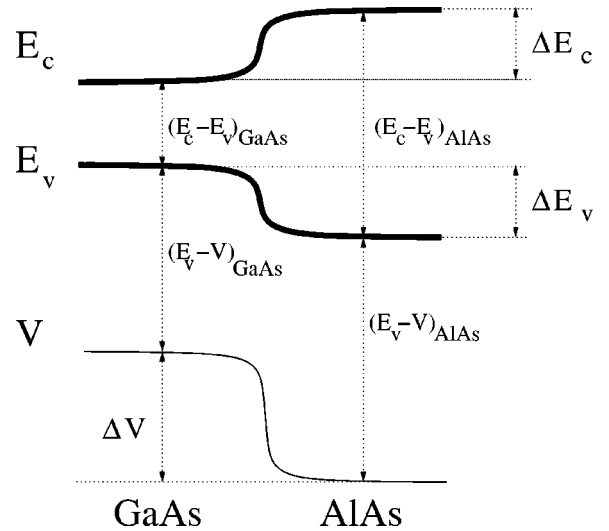


FIG. 12. GaAs/AlAs band alignment.

$$\Delta = \Delta E_v + \Delta V, \quad (9)$$

where ΔV is the offset between the AlAs and the GaAs electrostatic potentials calculated for an AlAs/GaAs heterostructure, and ΔE_v is the energy difference between the valence band tops, E_v , of the bulk materials. These are calculated from their electrostatic potential V ,

$$\Delta E_v = (E_v - V)_{\text{GaAs}} - (E_v - V)_{\text{AlAs}}. \quad (10)$$

Here we have constructed a supercell by stacking four AlAs cubic cells on top of four GaAs cubic cells, all with the same GaAs lattice constant (5.65 Å). Our calculations give a valence band offset of $\Delta = 0.405$ eV ($\Delta = 0.403$ eV if the total DFT potential is considered instead of the electrostatic one). This value for Δ is in very good agreement with both experimental results⁴⁷ and early DFT calculations.⁴⁸ The resulting GaAs/AlAs band alignment is shown in Fig. 12; it provides an additional confinement potential for holes in the GaAs region. Therefore a stronger ferromagnetic coupling is expected.

B. Electronic structure

Also in this case the band structure and the DFT potential are the main quantities to investigate. First we study the evolution of the electronic properties as a function of the AlAs fraction of the superlattice. We construct $\text{GaAs}_{(5-n)/2}/\text{AlAs}_n/\text{GaAs}_{(5-n)/2}/(\text{Ga,Mn})\text{As}_1$ superlattices, where the labels indicate the number of monolayers of the specific semiconductor. Note that the total number of monolayers in our supercell is six, and that the AlAs fraction is always located in the middle of the cell.

In Fig. 13 we present the band structure of a 50% DFH with Mn ions uniformly distributed in the plane (configuration FM_1), for the cases $n = 0, 1, 3, 5$. As usual we consider only the in plane directions.

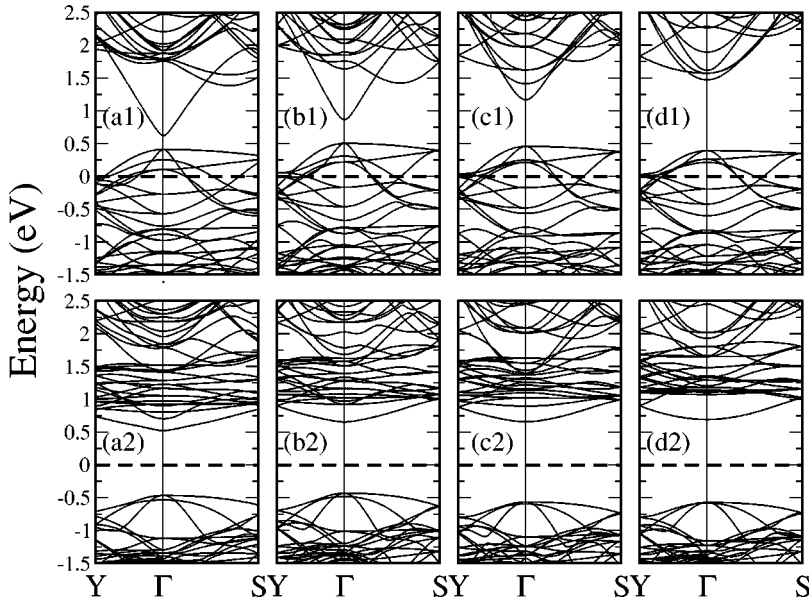


FIG. 13. Band structure of AlAs/GaAs/(Ga,Mn)As DFH as a function of the AlAs fraction: (a) $n=0$, (b) $n=1$, (c) $n=3$, (d) $n=5$. The top panels are for the majority spin band and the bottom for the minority. The horizontal line indicates the position of the Fermi level, which is set to $E_F=0$ eV.

From Fig. 13 we can see that the only appreciable change in the band structure as the AlAs fraction increases is an enhancement of the band gap. This, of course, reflects the different AlAs/GaAs ratios of the superlattices and the larger bandgap of AlAs compared with GaAs (our LDA values are 1.7 eV and 0.6 eV, respectively). For all the superlattices studied, the magnetic moment of the unit cell is $16\mu_B$ and the Mülliken analysis gives a Mn d occupation of ~ 4.7 and ~ 0.8 , respectively, for majority and minority spins. Such an occupation is independent of the AlAs fraction and suggests that Mn is always in a d^5 state plus an antiferromagnetically coupled hole, as in the case of GaAs/(Ga,Mn)As DFH.

A closer look at the band structure reveals another important feature. The spin splitting of the valence band top, $\Delta_v = E_v^\uparrow - E_v^\downarrow$, is a nonmonotonic function of the AlAs fraction, with values of 0.88 eV, 0.93 eV, 1.02 eV, and 0.96 eV for $n=0, 1, 3$, and 5, respectively. The initial increase is due to

the enhanced confinement of the free holes in the Mn region. In fact, the mean-field expression for the valence band top spin splitting is simply^{4,33}

$$\Delta_v = xN\beta\langle S \rangle, \quad (11)$$

where $N\beta$ is the p - d exchange constant, $\langle S \rangle$ is the mean spin [$\langle S \rangle = 5/2$ for (Ga,Mn)As], and x is the Mn concentration. The exchange constant $N\beta$ depends on the degree of overlap between the hole density and the Mn ions, and this is enhanced by hole confinement. Therefore we expect an increase of Δ_v when the AlAs fraction is increased. The case $n=5$ is different, since no GaAs region is left and the additional confinement of the hole in the Mn plane due to the AlAs/GaAs valence band offset is partially lost.

Another important quantity to investigate is the DFT total potential. In Fig. 14 we present the macroscopic average

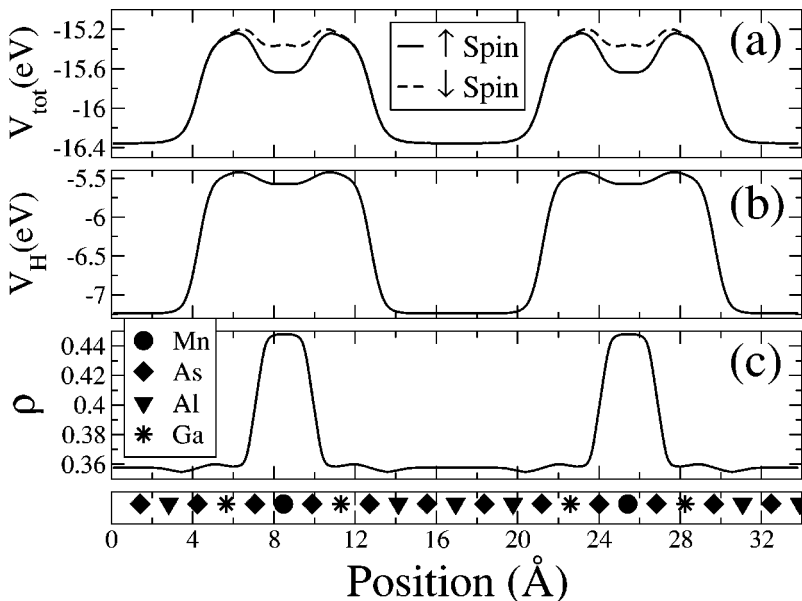


FIG. 14. Macroscopic average of (a) the total DFT potential, (b) the Hartree potential, and (c) the charge-density distribution as a function of the position along the superlattice direction. The system is a GaAs₁/AlAs₃/GaAs₁/(Ga,Mn)As₁ superlattice with 50% Mn uniformly distributed in the plane (configuration FM₁). Here we plot two superlattice periods.

TABLE III. J_1 , J_2 , J_3 and $x\sum_i J_i$ as a function of the number of the AlAs layers in the supercell. All the units are meV.

AlAs planes (n)	J_1	J_2	J_3	$x\sum_i J_i$
$n=0$	13.3	0.9	4.5	9.35
$n=2$	13.8	0.9	4.7	9.72
$n=3$	14.0	0.8	4.9	9.85
$n=5$	14.6	0.6	5.2	10.30

along the superlattice direction of the DFT and Hartree potentials, and the electronic charge density, for a 50% DFH (configuration FM₁), where we introduce three AlAs monolayers [GaAs₁/AlAs₃/GaAs₁/(Ga,Mn)As₁]. The figure shows that there is a large well for both majority and minority spin electrons in the AlAs region. This is mainly due to the Hartree component of the DFT potential and it is not spin sensitive. The width of this region depends on the thickness of the AlAs layer and plots for other values of n give similar results. If we interpret the macroscopic average of the DFT potential in the spirit of the envelope function approximation, we can conclude that new electrons coming from intrinsic donors will be preferentially localized in the AlAs region. Therefore the ferromagnetism in AlAs/(Ga,Mn)As DFH appears to be more robust against electron doping than that in GaAs/(Ga,Mn)As DFH. This is consistent with the rather large T_C found in AlAs/GaAs/(Ga,Mn)As DFH.^{18,19}

C. Fit to the Heisenberg model

As in the case of (Ga,Mn)As/GaAs DFH we investigate the strength of the ferromagnetic coupling by fitting our total energy calculation to third nearest-neighbor Heisenberg model. We consider only the case of 50% Mn in the plane and we study the dependence of the coupling constants on the number of AlAs layers in the supercell. The results of our fit are shown in Table III.

From the table one can conclude that the total strength of the coupling, which is proportional to T_C , increases as a function of the AlAs fraction. This is consistent with an enhanced ferromagnetic coupling between the holes and the Mn ions due to confinement. Therefore in the absence of intrinsic defects, AlAs/(Ga,Mn)As DFH are more promising than GaAs/(Ga,Mn)As DFH as high T_C DMS. It is also interesting to note that the different exchange constants behave in a different way when the AlAs fraction is increased: J_1 and J_3 are enhanced and J_2 is reduced. This behavior is not surprising within a carrier mediated ferromagnetism model (e.g., RKKY), since an increase of the AlAs fraction changes the value of the Fermi wave vector, and therefore the period of the exchange coupling.

Having established that defect-free AlAs/(Ga,Mn)As DFH present higher T_C than their GaAs/(Ga,Mn)As counterparts, we finally investigate the stability of the ferromagnetic coupling against the presence of As antisites. As usual, we introduce one As_{Ga} per unit cell at various positions along the superlattice direction. Here we consider two limiting cases: (1) $n=3$ and the As antisite is located in one of the GaAs

planes adjacent to the Mn plane, (2) $n=5$ and the As antisite is located in the middle of the unit cell (in the AlAs region).

In the first case, we find the coupling constants to be $J_1=7.0$ meV, $J_2=0.0$ meV, $J_3=2.9$ meV, $x\sum_i J_i=4.95$ meV. This is a considerable reduction of the ferromagnetic coupling with respect to the defect-free case. In this case the values of the coupling constants are almost identical to those of GaAs/(Ga,Mn)As DFH in which an antisite is introduced at the same position (in Fig. 11 the As_{Ga} position is 1/6). Therefore, if the As antisites are introduced in the GaAs region, there will be no beneficial effects from the AlAs/GaAs band alignment.

The situation is rather different in the second case where the As antisites are introduced in the AlAs layer. Now the coupling constants are $J_1=10.1$ meV, $J_2=-0.1$ meV, $J_3=4.4$ meV, and the reduction of the total coupling $x\sum_i J_i$ with respect to the defect-free case is only of about 30%. Interestingly, J_2 now assumes a negative value, suggesting some possible frustration even at low temperature.

In conclusion, AlAs/GaAs/(Ga,Mn)As DFH have stronger ferromagnetic interaction between the Mn ions than GaAs/(Ga,Mn)As DFH. Moreover, in the case that intrinsic defects are kept into the AlAs region, the ferromagnetic order is more robust against hole compensation.

VI. CONCLUSIONS

We have performed an extensive theoretical study of the electronic, magnetic, and transport properties of GaAs/(Ga,Mn)As and AlAs/GaAs/(Ga,Mn)As DFH, using DFT within LSDA.

We find that GaAs/(Ga,Mn)As DFH show a half-metal band structure with metallic conductance in the Mn plane. The macroscopic average of the DFT potential indicates a selective confinement of the spin holes in the Mn planes and the Mn-Mn ferromagnetic interaction is nonmonotonically dependent on the Mn concentration.

When compensating defects such as As antisites are introduced, the half-metallic state is lost and conducting channels appear in the minority spin band. These are due to hopping conductance through localized As_{Ga} states. However, at least when the As antisites are far from the Mn planes, there is a spatial separation of the two spin currents with a metallic majority spin current located in the Mn planes, and an hopping-type minority spin current located primarily in the GaAs region. These differences in the type of transport for the two spin bands are magnified in the diffusive limit, for which we calculate a spin polarization of about 80%. Finally, the presence of As antisites generally weakens the ferromagnetic interaction, and local antiferromagnetic coupling between Mn ions is possible at low temperature.

With all these results in hand we conclude that GaAs/(Ga,Mn)As DFH behave as dirty planar metals, where the strength of the ferromagnetic coupling depends strongly on the amount and the position of the intrinsic defects.

Finally, we have investigated the effect of additional confinement by studying AlAs/GaAs/(Ga,Mn)As DFH. In this case our accurate total energy calculations confirm that the band offset between GaAs and AlAs strongly confines the

holes in the Mn region resulting in a larger Mn-Mn coupling. In addition, we find that these structures are less sensitive to the presence of As antisites than the simpler GaAs/(Ga,Mn)As DFH.

We therefore conclude that band engineering, selective doping, and the ability to control the actual position of As antisites or other compensating defects are the main keys to obtain room-temperature ferromagnetism in DFH.

ACKNOWLEDGMENTS

This work was supported by Enterprise Ireland under Grant No. EI-Sc/2002-10. The calculations have been carried out using the computational facilities of the Trinity Center for High Performance Computing (TCHPC). Useful discussions with N.A. Spaldin and J.M.D. Coey are kindly acknowledged.

*Electronic address: sanvitos@tcd.ie

- ¹H. Ohno, A. Shen, F. Matsukura, A. Oiwa, A. Endo, and S. Kutsumoto, *Appl. Phys. Lett.* **69**, 363 (1996).
- ²H. Ohno, *J. Magn. Magn. Mater.* **200**, 110 (1999).
- ³H. Ohno, *Science* **281**, 951 (1998).
- ⁴T. Dietl, H. Ohno, F. Matsukura, J. Cibèrt, and D. Ferrand, *Science* **287**, 1019 (2000).
- ⁵G. Prinz, *Science* **282**, 1660 (1998); *Phys. Today* **48** (4), 58 (1995).
- ⁶Y. Ohno, D.K. Young, B. Beschoten, F. Matsukura, H. Ohno, and D.D. Awschalom, *Nature (London)* **402**, 790 (1999).
- ⁷H. Ohno, D. Chiba, F. Matsukura, T. Omiya, E. Abe, T. Dietl, Y. Ohno, and K. Ohtani, *Nature (London)* **408**, 944 (2000).
- ⁸D.P. Di Vincenzo, *Science* **270**, 255 (1995).
- ⁹K.W. Edmonds, K.Y. Wang, R.P. Champion, A.C. Neumann, N.R.S. Farley, B.L. Gallagher, and C.T. Foxon, *Appl. Phys. Lett.* **81**, 4991 (2002).
- ¹⁰K.C. Ku, S.J. Potashnik, R.F. Wang, S.H. Chun, P. Schiffer, N. Samarth, M.J. Seong, A. Mascarenhas, E. Johnston-Halperin, R.C. Myers, A.C. Gossard, and D.D. Awschalom, *Appl. Phys. Lett.* **82**, 2302 (2003).
- ¹¹R.K. Kawakami, E. Johnston-Halperin, L.F. Chen, M. Hanson, N. Guébels, J.S. Speck, A.C. Gossard, and D.D. Awschalom, *Appl. Phys. Lett.* **77**, 2379 (2000).
- ¹²G. Zanelatto, T. Kreutz, R.K. Kawakami, E. Johnston-Halperin, E. Gwinn, D.D. Awschalom, and A.C. Gossard, *Bull. Am. Phys. Soc.* **46** (1), 509 (2001).
- ¹³T. Kreutz, G. Zanelatto, R.K. Kawakami, E. Johnston-Halperin, E. Gwinn, D.D. Awschalom, and A.C. Gossard, *Bull. Am. Phys. Soc.* **46** (1), 510 (2001).
- ¹⁴H. Luo, B.D. McCombe, M.H. Na, K. Mooney, F. Lehmann, X. Chen, M. Cheon, S.M. Wang, Y. Sasaki, X. Liu, and J.K. Furdyna, *Physica E (Amsterdam)* **12**, 366 (2002).
- ¹⁵B.D. McCombe, M.H. Na, X. Chen, M. Cheon, S. Wang, H. Luo, X. Liu, Y. Sasaki, T. Wojtowicz, J.K. Furdyna, S.J. Potashnik, and P. Schiffer, *Physica E (Amsterdam)* **16**, 90 (2003).
- ¹⁶T.C. Kreutz, G. Zanelatto, E.G. Gwinn, and A.C. Gossard, *Appl. Phys. Lett.* **81**, 4766 (2002).
- ¹⁷X. Chen, M. Na, M. Cheon, S. Wang, H. Luo, B.D. McCombe, X. Liu, Y. Sasaki, T. Wojtowicz, J.K. Furdyna, S.J. Potashnik, and P. Schiffer, *Appl. Phys. Lett.* **81**, 511 (2002).
- ¹⁸A.M. Nazmul, S. Sugahara, and M. Tanaka, *Phys. Rev. B* **67**, 241308 (2003); *Appl. Phys. Lett.* **80**, 3120 (2002).
- ¹⁹T. Wojtowicz, W.L. Lim, X. Liu, M. Dobrowolska, J.K. Furdyna, K.M. Yu, W. Walukiewicz, I. Vurgaftman, and J.R. Meyer, *cond-mat/0305047* (unpublished).
- ²⁰J.P. Noh, F. Shimogishi, and N. Otsuka, *Phys. Rev. B* **67**, 075309 (2003).
- ²¹I. Vurgaftman and J.R. Meyer, *Phys. Rev. B* **64**, 245207 (2001).
- ²²J. Fernández-Rossier and L.J. Sham, *Phys. Rev. B* **64**, 235323 (2001).
- ²³S. Sanvito and N.A. Hill, *Phys. Rev. Lett.* **87**, 267202 (2001).
- ²⁴H. Hohenberg and W. Kohn, *Phys. Rev.* **136**, B864 (1964); W. Kohn and L.J. Sham, *Phys. Rev.* **140**, A1133 (1965).
- ²⁵S. Sanvito, G. Theurich, and N.A. Hill, *J. Supercond.* **15**, 85 (2002).
- ²⁶A. Filippetti, N.A. Spaldin, and S. Sanvito, *cond-mat/0302178* (unpublished).
- ²⁷P. Ordejón, D. Sánchez-Portal, E. Artacho, and J.M. Soler, <http://www.uam.es/departamentos/ciencias/fismateria/c/siesta>
- ²⁸J.M. Soler, E. Artacho, J.D. Gale, A. García, J. Junquera, P. Ordejón, and D. Sánchez-Portal, *J. Phys.: Condens. Matter* **14**, 2745 (2002), and references therein.
- ²⁹N. Troullier and J.L. Martins, *Phys. Rev. B* **43**, 1993 (1991).
- ³⁰S.G. Louie, S. Froyen, and M.L. Cohen, *Phys. Rev. B* **26**, 1738 (1982).
- ³¹L. Kleinman and D.M. Bylander, *Phys. Rev. Lett.* **48**, 1425 (1982).
- ³²E. Artacho, D. Sanchez-Portal, P. Ordejón, A. Garcia, and J.M. Soler, *Phys. Status Solidi* **215**, 809 (1999).
- ³³S. Sanvito, P. Ordejón, and N.A. Hill, *Phys. Rev. B* **63**, 165206 (2000).
- ³⁴R.S. Mülliken, *J. Chem. Phys.* **23**, 1833 (1955); **23**, 1841 (1955).
- ³⁵S. Sanvito and N.A. Hill, *Appl. Phys. Lett.* **78**, 3493 (2001).
- ³⁶S. Baroni, R. Resta, A. Baldereschi, and M. Peressi, in *Spectroscopy of Semiconductor Microstructures*, edited by G. Fasol, A. Fasolino, and P. Lugli (Plenum, New York, 1989), p. 251.
- ³⁷T. Jungwirth, W.A. Atkinson, B.H. Lee, and A.H. MacDonald, *Phys. Rev. B* **59**, 9818 (1999).
- ³⁸M. van Schilfgaarde and O.N. Mryasov, *Phys. Rev. B* **63**, 233205 (2001).
- ³⁹T. Jungwirth, J. König, J. Sinova, J. Kucera, and A.H. MacDonald, *Phys. Rev. B* **66**, 012402 (2002).
- ⁴⁰M. Berciu and R.N. Bhatt, *Phys. Rev. B* **66**, 085207 (2002).
- ⁴¹S. Sanvito, C.J. Lambert, J.H. Jefferson, and A.M. Bratkovsky, *Phys. Rev. B* **59**, 11 936 (1999).
- ⁴²M. Büttiker, Y. Imry, R. Landauer, and S. Pinhas, *Phys. Rev. B* **31**, 6207 (1985).
- ⁴³K.M. Yu, T. Walukiewicz, T. Wojtowicz, I. Kuryliszyn, X. Liu, Y. Sasaki, and J.K. Furdyna, *Phys. Rev. B* **65**, 201303(R) (2002).

- ⁴⁴J. Blinowski and P. Kacman, Phys. Rev. B **67**, 121204(R) (2003).
- ⁴⁵S. Sanvito and N.A. Hill, J. Magn. Magn. Mater. **242–245**, 441 (2002).
- ⁴⁶I.I. Mazin, Phys. Rev. Lett. **83**, 1427 (1999).
- ⁴⁷L. Sorba, G. Bratina, G. Ceccone, A. Antonini, J.F. Walker, M. Micovic, and A. Franciosi, Phys. Rev. B **43**, 2450 (1991).
- ⁴⁸R.H. Miwa and A.C. Ferraz, Phys. Rev. B **59**, 12 499 (1999).